

# Sketching the spatial disparities in heatwave trends by changing atmospheric teleconnections in the Northern Hemisphere

---

Received: 12 February 2024

---

Accepted: 2 September 2024

---

Published online: 13 September 2024

---

 Check for updates

---

Fenyng Cai<sup>1,2</sup>, Caihong Liu<sup>3</sup>, Dieter Gerten<sup>1,2</sup>, Song Yang<sup>4,5</sup>✉, Tuantuan Zhang<sup>4,5</sup>✉, Kaiwen Li<sup>1,6,7</sup> & Jürgen Kurths<sup>1,8,9</sup>

Pronounced spatial disparities in heatwave trends are bound up with a diversity of atmospheric signals with complex variations, including different phases and wavenumbers. However, assessing their relationships quantitatively remains a challenging problem. Here, we use a network-searching approach to identify the strengths of heatwave-related atmospheric teleconnections (AT) with ERA5 reanalysis data. This way, we quantify the close links between heatwave intensity and AT in the Northern Hemisphere. Approximately half of the interannual variability of heatwaves is explained and nearly 80% of the zonally asymmetric trend signs are estimated correctly by the AT changes in the mid-latitudes. We also uncover that the likelihood of extremely hot summers has increased sharply by a factor of 4.5 after 2000 over areas with enhanced AT, but remained almost unchanged over the areas with attenuated AT. Furthermore, reproducing Eastern European heatwave trends among various models of the Coupled Model Intercomparison Project Phase 6 largely depends on the simulated Eurasian AT changes, highlighting the potentially significant impact of AT shifts on the simulation and projection of heatwaves.

Increasing and intensifying heatwaves observed in historical records and projected for the warming future have drawn worldwide concerns<sup>1–8</sup>. In particular, overwhelming social and economic consequences were caused by the recent more frequent record-breaking heatwaves over the regions with accelerated warming<sup>9–17</sup>. Over 60,000 heat-related deaths were estimated in 35 European countries when wide-spreading extreme heatwaves occurred in the summer of 2022<sup>9</sup>. Record-breaking temperature in July 2021, even 20°C above normal in some American cities, caused >1,400 deaths, numerous large-scale wildfires, and spreading smoke pollution over Western North America<sup>10–13</sup>. Such disproportionate threats of heatwaves<sup>6,15–17</sup> highlight

the necessity of disentangling the origin of amplified warming risks over the hotspot regions.

Pronounced spatial dissimilarities of heatwave trends have been detected recently<sup>15–18</sup> (also see Supplementary Fig. S1a). For the hotspot regions such as Europe and Western North America, increasing trends in heatwave intensities are twice as strong as in the zonal means, whereas decreasing trends are observed in Eastern North America and northern India (see Supplementary Fig. S1a). The spatially nonuniform heatwave trends have been largely attributed to the changes in atmospheric circulation patterns<sup>16–18</sup>. In particular, the trends toward accelerated heatwaves in Europe appear to be tightly linked to more

---

<sup>1</sup>Potsdam Institute for Climate Impact Research (PIK), Member of the Leibniz Association, 14473 Potsdam, Germany. <sup>2</sup>Department of Geography, Humboldt-Universität zu Berlin, 10099 Berlin, Germany. <sup>3</sup>Department of Water and Climate Risk, Institute for Environmental Studies, Vrije University Amsterdam, 1087HV Amsterdam, Netherlands. <sup>4</sup>School of Atmospheric Sciences, Sun Yat-sen University, and Southern Marine Science and Engineering Guangdong Laboratory (Zhuhai), 519082 Zhuhai, China. <sup>5</sup>Guangdong Province Key Laboratory for Climate Change and Natural Disaster Studies, Sun Yat-sen University, 519082 Zhuhai, China. <sup>6</sup>School of National Safety and Emergency Management, Beijing Normal University, 100875 Beijing, China. <sup>7</sup>Faculty of Geographical Science, Beijing Normal University, 100875 Beijing, China. <sup>8</sup>Department of Physics, Humboldt-Universität zu Berlin, 10099 Berlin, Germany. <sup>9</sup>School of Mathematical Sciences, SCMS, and CCSB, Fudan University, 200433 Shanghai, China. ✉e-mail: [yangsong3@mail.sysu.edu.cn](mailto:yangsong3@mail.sysu.edu.cn); [zhangtt75@mail.sysu.edu.cn](mailto:zhangtt75@mail.sysu.edu.cn)

persistent Eurasian double jet streams<sup>16</sup> and intensified Silk Road pattern<sup>17,18</sup>. Double-jet configurations, characterized by a split in the Eurasian jet stream into two separated zonal wind centers, are linked to high occurrences of blocking anticyclones and substantial positive trends in heatwave intensity over Europe<sup>16</sup>. Similar blocking anticyclone over Eastern Europe, as a part of alternative Eurasian anticyclonic and cyclonic circulation anomalies during the negative phase of the Silk Road pattern, is conducive to surface warming over Europe<sup>17,18</sup>.

Previous studies have been focused mainly on the impacts of a specific atmospheric circulation phenomenon<sup>13,16,19</sup>, in particular blocking anticyclones or double jets, or a few well-known atmospheric teleconnection patterns<sup>17,18,20–23</sup> (AT; e.g. the Silk Road pattern and the circumglobal Rossby waves with wavenumbers 3, 5, and 7). However, climate extremes over different areas are in a complex manner related to a diversity of atmospheric signals with dissimilar variations and changes<sup>17,18,24,25</sup>. It is hard to examine thoroughly the large-scale heterogeneous heatwave trends in the Northern Hemisphere based on a single AT system. Furthermore, state-of-the-art climate models cannot reproduce the accelerated heatwave trends over some hotspots like Western Europe<sup>26</sup>. Until now, we lack a universal and quantitative understanding of the linkage between spatially heterogeneous summertime heatwave intensity trends and nonuniform AT changes in the Northern Hemisphere.

The framework of complex networks has been widely used in extreme weather analysis, including the synchronization and propagation analysis of extreme rainfall<sup>27–29</sup>, heatwaves<sup>30–32</sup>, and droughts<sup>33</sup>. However, only few of the extreme weather network analysis have involved the complex atmospheric circulation changes. In this study, the geographical features of heatwave-related AT are investigated by analyzing heatwave and atmospheric geopotential height extreme networks, using daily maximum near-surface temperature ( $T_{\max}$ ) and geopotential height at 500 hPa during the time period of 1979–2022 from the ERA5 reanalysis dataset<sup>34</sup> (see Methods for details). For each heatwave grid cell, we search two most-connected high-pressure grid cells and two low-pressure grid cells, which indicate the information about heatwave-related AT. The searching algorithm for most-connected grid cells is based on the strongest interannual correlations and the highest daily concurrences between heatwaves and pressure extremes. A quantitative heatwave-related AT index is retrieved at each grid cell by averaging the most-connected local high-pressure and remote low-pressure intensities (see Methods for details). A flow chart (see Supplementary Fig. S2) including several steps with details provides a comprehensive understanding of network analysis. The contribution of AT shifts to the spatially heterogeneous trends in heatwaves is quantified with ERA5 dataset and further verified by the Coupled Model Intercomparison Project Phase 6 (CMIP6) models<sup>35</sup>. This framework enables us to retrieve the quantitative linkage between heatwave trends and AT changes. It will provide substantial insights into the simulation and even the future projection of heatwaves.

## Results

### Concurrent weather extremes in a framework of network analysis

Six climate networks based on the co-variability among heatwaves, cold extremes, high-pressure extremes, and low-pressure extremes are constructed (see Methods for details). The link strengths in the networks are identified as the temporal similarity among several types of climate extremes over different grid cells. In particular, the similarity could be calculated in two ways: the number of daily concurrences between different extremes, and the Pearson's correlation coefficients between different yearly time series of extreme intensities. We analyze the spatial features (i.e., the geographical distances) of heatwave-AT relationships by displaying the distance distribution of the strong links

in six different climate networks (Fig. 1). The strength of a link between two grid cells in these networks is determined by the temporal similarity between climate extremes occurring in the two grid cells. For four networks (heat-heat, heat-cold, heat-high, and heat-low), the number of daily concurrences (see Supplementary Fig. S3) is used to represent the similarity, while for the other two networks (heat-high and heat-low), the Pearson's correlation coefficients between different yearly time series of detrended extreme intensities are calculated to identify the link strength (see Methods for details).

According to our objective and quantitative network analysis, the occurrences of heatwaves in the neighborhoods within 1500 km are highly simultaneous, but the concurrences decrease sharply with increasing distance (Fig. 1a). That is, heatwaves generally occur concurrently with large-scale tropospheric blockings/anticyclones, which can cause sinking motions and cloud reduction, conducive to surface warming<sup>24,25,36–39</sup>. The concurrences of weather extremes in two remote grid cells are now further investigated since long-distance connections hint at signal propagation within the atmospheric circulation system. We do not consider time delay when counting the number of concurrences between weather extremes over two grid cells for simplifying computation (see Supplementary Fig. S3; see Methods for details), and this is enough to retrieve the major geographical features shown in Fig. 1. It is noteworthy that from our results for the Northern Hemisphere, the frequency of remote heatwave concurrences is higher in a geographical distance of nearly 5200 km than for other distances (Fig. 1a). The distance distribution of heatwave concurrences is quite similar to that of extreme rainfall synchronizations<sup>29</sup>, implying analogous AT effects on extreme weather teleconnection. On the other hand, heatwave and cold extremes most likely appear synchronously and remotely with a distance of about 2700 km (Fig. 1a).

Remote simultaneous occurrences of weather extremes are largely modulated by AT, featured by Rossby wave trains with alternative atmospheric low-pressure and high-pressure anomalies<sup>21,22</sup>. From the network analysis of daily concurrent heatwave and pressure extreme (Fig. 1b), heatwaves tend to occur simultaneously with local high-pressure extremes (<1000 km), remote low-pressure extremes with a distance of ~2700 km, and remote high-pressure extremes with a distance of ~5700 km. The geographical distance distributions in the interannual correlation network are similar to those in the daily concurrence network (Fig. 1b vs Fig. 1c), implying a consistency between daily and interannual time scales. In particular, the remote regions with heatwaves occurring nearly-simultaneously, such as Eastern Europe and Eastern Asia, also exhibit high co-variability of heatwave activities on the interannual time scales<sup>17,18,38,39</sup>.

European heatwaves could serve as examples to display physical links between heatwaves, cold extremes, high-pressure extremes, and low-pressure extremes. When Eastern European heatwaves occur (see Methods for the composite analysis for regional heatwave events), high-temperature and high-pressure anomalies are observed synchronously 5200 km away over Eastern and Northeastern Asia (Fig. 2a), as reported in previous studies<sup>22,38,39</sup>. In the geometric region between the two remote heatwave centers, cold extremes are observed over Ural-central Asia (Fig. 2a). The distance from Eastern Europe to Ural-central Asia is approximately 2700 km, which is about half of the length for recurrent circumglobal Rossby wave patterns with wavenumbers 5 and 7 in the northern mid-latitudes<sup>21,22</sup>. An eastward propagating atmospheric wave train (Fig. 2b), represented by alternative high-pressure and low-pressure anomalies, bridges the concurrences of remote heatwaves and cold extremes. Similarly, the occurrences of Western European heatwaves (see Methods for details) are accompanied by a southeastward-eastward propagating Rossby wave train<sup>40</sup>, which includes low-pressure anomalies over the Northeastern Atlantic, the Northern Africa, and the Ural, and high-pressure anomalies over Western Europe and central Asia-central Russia (Fig. 2d, e). The geographical distance between Western Europe and upstream low-

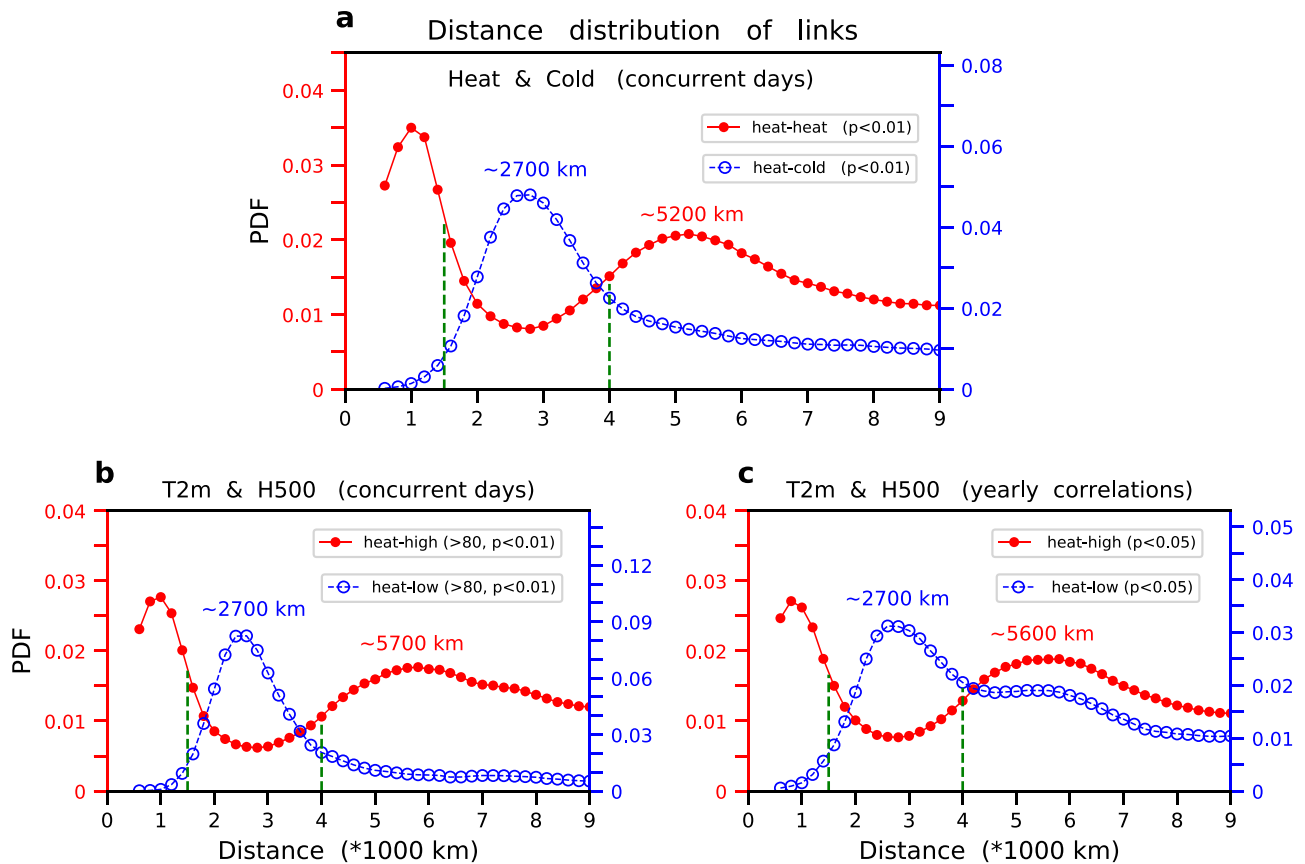


**Fig. 1 | Geographical distances of weather extremes.** Probability density function (PDF) for the distance of significant links in (a) heat-heat daily concurrence networks (red line with solid circles) and heat-cold daily concurrence networks (blue line with hollow circles), (b) heat-high daily concurrence networks (red line with solid circles) and heat-low daily concurrence networks (blue line with hollow circles), and (c) heat-high interannual correlation networks (red line with solid circles) and heat-low interannual correlation networks (blue line with hollow circles).

Networks in (b, c) are constructed between weather extremes based on air temperature at 2 m ( $T_{2m}$ ) and geopotential height at 500 hPa ( $H500$ ). The significant p-values are shown in the upper right labels in (a–c). The links with link strengths  $L_{(a,b)} \leq 80$  for the two networks in (b) are considered as weak links and thus removed. The vertical dashed green lines in (a–c) denote the distances of 1500 km and 4000 km.

pressure center over the Northeastern Atlantic is similarly close to 2700 km (Fig. 2d). Cross-degree centralities inside Western European and Eastern European heatwaves reinforce that European heatwaves are connected to local high-pressure extremes (<1000 km) and remote low-pressure extremes in a distance of ~2700 km (Fig. 2c and f). It is emphasized that the heatwave-related AT pattern widely applies to regions with different latitudes and longitudes in the Northern Hemisphere (see Supplementary Figs. S4 and S5), even though the distance for the maximum remote high-pressure center varies in a range between 5000 km and 6000 km based on different thresholds (see Supplementary Fig. S6). The strongest concurrences between heatwaves and low-pressure extremes are observed with a distance of 1500–4000 km for above 85 % of the land area in the middle-high latitudes (see Supplementary Fig. S7). Overall, the geographical features obtained from the climate network analysis are spatially identified and visualized in realistic large-scale heatwave events, instead of being spurious statistical characteristics.

### Quantifying the contribution of AT shifts to spatially heterogeneous trends in heatwaves

A quantity of particular interest is to assess the strengths of grid-based heatwave-related AT. After retrieving the AT intensity with spatial-temporal variations, it is feasible to quantify the linkage between zonally asymmetric heatwave trends and AT changes.

Including the geographical features of heatwave-AT linkage, we identify the intensity of AT for heatwaves at each grid cell as the mean

intensity of local (<1500 km) most-connected high-pressure extremes and remote (1500–4000 km) most-connected low-pressure extremes (see Methods for details). The explained variances of heatwave cumulative intensity (HWI) linked to the AT intensity after being removed linear temporal trends are evaluated (Fig. 2g). For those regions with high AT-HWI correlations, AT accounts for over 50% of the HWI interannual variability over Europe, Northeastern Asia, northern Africa, and Northwestern North America (Fig. 2g). For the zonal median estimate of AT-HWI relationships in the middle-higher latitudes, approximately 45% of the heatwave interannual variability is attributable to AT variations, higher than that over the subtropics (Fig. 2h). The high linkage between HWI and AT is mainly due to the significant relationship between HWI and local high-pressure intensities (Fig. 2h; see Supplementary information text and Fig. S8). Nevertheless, dipolar AT index directly including remote low-pressure intensities, exhibits a stronger interannual linkage with heatwaves in the Northern Hemisphere, compared with the only local high-pressure index (see Supplementary information text and Fig. S8).

Worldwide increasing yet spatially heterogeneous trends in heatwaves have been observed during the past four decades (see Supplementary Fig. S1). In particular, more pronounced upward trends appear in the middle-higher latitudes with a zonally asymmetric feature (see Supplementary Fig. S1). The strong linkage between heatwaves and AT may assist a thorough understanding of the spatially heterogeneous HWI trends in the Northern Hemisphere. To retrieve this spatial heterogeneity, the zonally asymmetric trends in HWI are

## Composite for Eastern and Western European Heatwaves

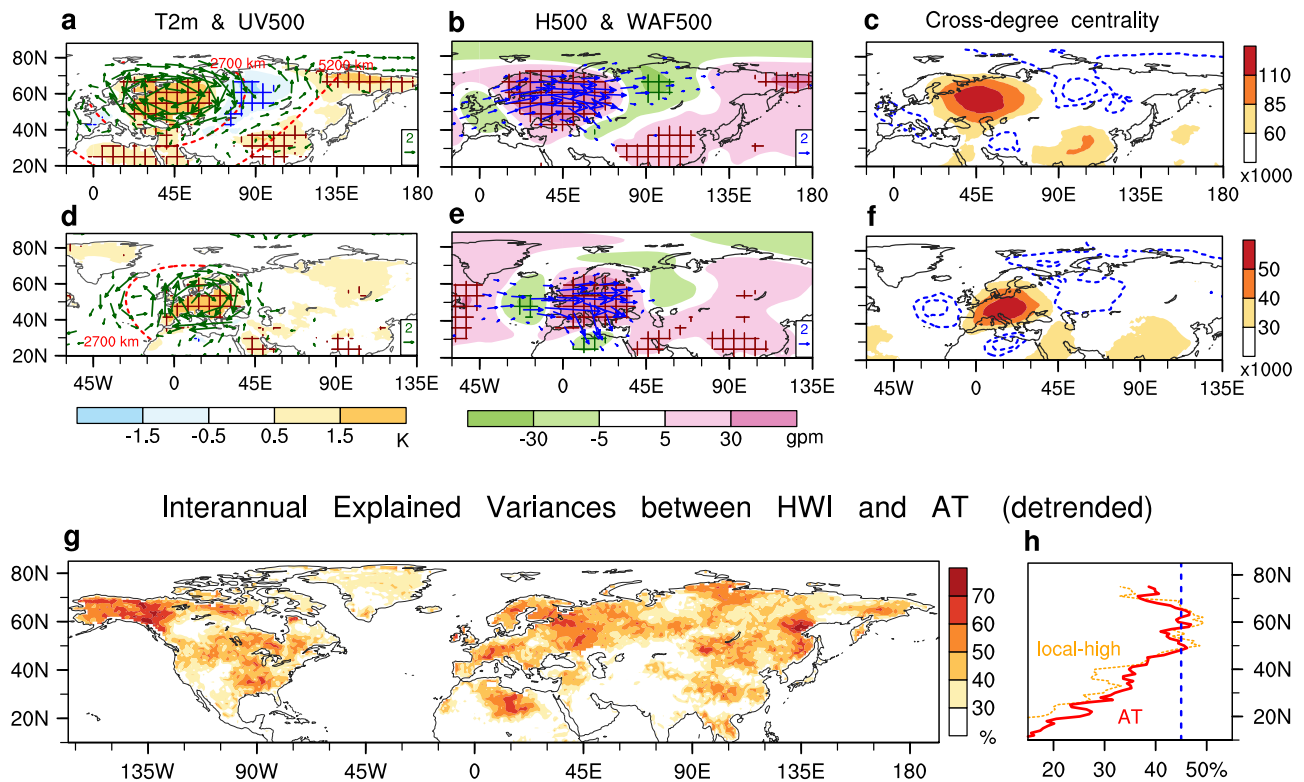


**Fig. 2 | Linkage between heatwaves and atmospheric teleconnections (AT).** Composite anomalies of (a, d) air temperature at 2 m ( $T_{2m}$ ; shadings; units: K) and atmospheric circulations at 500 hPa (UV500; vectors; units:  $m s^{-1}$ ), and (b, e) geopotential height (H500; shadings; units: gpm) and wave flux activity (WAF500; vectors; units:  $m^2 s^{-2}$ ) at 500 hPa. a, b are the composite anomalies for Eastern European heatwave events, while (d, e) are for Western European heatwave events. Cross-degree centrality of high-pressure extremes (shadings; units:  $\times 1000$ ) inside (c) Eastern European heatwaves and (f) Western European heatwaves. Cross-degree centrality of low-pressure extremes (blue dashed contours) for Eastern European heatwaves (shown at 42,000 and 50,000) and Western European heatwaves (shown at 21,000 and 25,000) are also plotted in (c) and (f), respectively. g Explained variance ( $R^2$ ) of yearly heatwave cumulative intensity (HWI) by AT, and

h the zonal median in explained variance (red solid line).  $R$  is the correlation coefficient between the yearly detrended time series of HWI and AT at each grid cell. The zonal median in explained variance between HWI and similar AT index using only local high-pressure intensities is also plotted as orange dashed line in (h). Significant values ( $p < 0.05$ ) are hatched and insignificant vectors are not plotted in (a, b) and (d, e). The wave activity fluxes are not shown when both directions of the values are less than  $0.5 m^2 s^{-2}$  or both wind component ( $u$  and  $v$ ) anomalies are insignificant. The red dashed lines in (a) and (d) denote the regions that are 2700 km and 5200 km far away from the centers of Eastern and Western European land areas, respectively. Yearly explained variances in (g) are positive over all grid cells and significant ( $R^2 > 0.147, p < 0.01$ ) over 99.8% of the land areas.

defined as the zonal deviations from the zonal mean (Fig. 3a; see Methods for details), in which positive deviations signify accelerated upward trends and negative ones indicate mitigated trends. The areas with accelerated trends in heatwaves include Europe, Western North America, Eastern Asia, and Northeastern Asia, while the areas with mitigated trends comprise central Russia, South Asia, and Eastern and Northwestern North America (Fig. 3a), in accordance with previous studies<sup>6,15–18</sup>.

To quantify the contribution from AT, the HWI trend is further estimated using a linear regression model based on the relationship between HWI and AT in each grid cell (see Methods for details). The estimated trends in HWI exhibit a high coincidence with the observed zonally asymmetric trends in HWI, with a spatial correlation coefficient ( $R$ ) up to 0.46 ( $p < 0.001$ ) and same signs over nearly 80% of the mid-latitude land areas near  $50^\circ N$  (Fig. 3a, b, and d). It is interesting to emphasize that accelerated and mitigated trends in HWI are linked to intensified and weakened AT, respectively.

Regional averaged zonally asymmetric trends in HWI and their estimated trends by AT changes are shown in Fig. 3c. In particular, the amplified AT explains up to two thirds of the zonally asymmetric trend over Europe, with a relatively higher contribution over Eastern Europe (70%) and a relatively lower one over Western

Europe (52%). Above-observed trends are estimated by AT over Eastern Asia (118%), probably due to the offset in AT-induced HWI increase trends by anthropogenic aerosol emissions over Eastern Asia<sup>41</sup>. The HWI asymmetric trend estimated by AT is very close to the observed trend over Northeastern Asia. In addition, about one third of the asymmetric trends are estimated over Northwestern North America, Eastern North America, and South Asia-central Asia due to the changes in AT. The upward and downward trends in AT are significant over these regions, except Northeastern Asia (Fig. 3c).

The changes in the mid-latitude HWI between 1979–2000 (P1) and 2001–2022 (P2) are further shown in Fig. 3e–g. The likelihood of high HWI years (the normalized value  $> 2$ ) tripled from 5.6% in the P1 to nearly 20% in the P2 (Fig. 3e). The changes in the occurrences of hot summers exhibit considerable disparities between regions (grid cells) with amplified AT (estimated HWI trends  $> 2$ ) and weakened AT (estimated HWI trends  $< -2$ ). The likelihood of the hottest -5% summers (the normalized observed HWI  $> 2$ ) has increased sharply by a factor of 4.5 from 5.4% to 24.4% for the areas with intensified AT (Fig. 3f), but remaining roughly unchanged for the regions with attenuated AT (Fig. 3g). Pronounced discrepancies in heatwave changes indicate concerns about the divergent future projections of heatwave intensity,

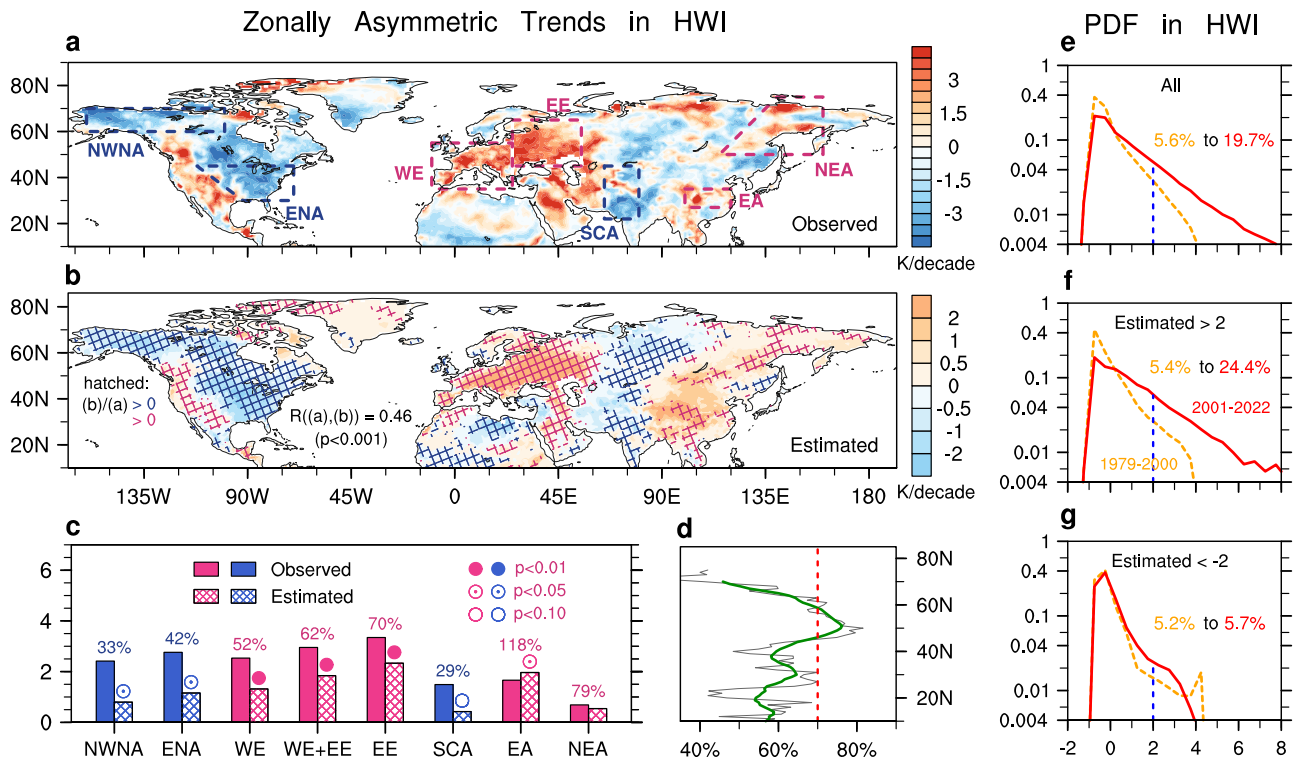


**Fig. 3 | Zonally asymmetric trends in heatwave cumulative intensity (HWI) attributable to atmospheric teleconnections (AT).** **a** Observed zonally asymmetric trends (observed trends minus their zonal mean) in HWI. **b** Estimated HWI trends by AT. **c** Regional observed (filled bars) and estimated (hatched bars) zonally asymmetric trends in HWI averaged over Northwestern North America (NWNA), Eastern North America (ENA), Western Europe (WE), Europe (including Western Europe and Eastern Europe), Eastern Europe (EE), South Asia-central Asia (SCA), Eastern Asia (EA), and Northeastern Asia (NEA). **d** Proportion (units: %) of land area (gray thin line) with the same signs between observed zonally asymmetric trend and estimated trend, and its 11-degree running average (green thick line). Probability density function (PDF; units: 1) of normalized HWI during the periods of

1979–2000 (orange dashed lines) and 2001–2022 (red solid lines) in **(e)** all grid cells, **(f)** grid cells where estimated trend is greater than 2, and **(g)** grid cells where estimated trend is less than -2, in mid-latitude land areas (40°–65°N). Units of HWI trend in **(a–c)** are K decade<sup>-1</sup>. Red (blue) hatched areas in **(b)** represent the areas with correct signs estimated by AT with accelerated (mitigated) HWI trends. The signs of negative observed zonally asymmetric and estimated trends (blue bars) are reversed in **(c)**. Colored solid, half solid, and hollow circles in **(c)** denote the trends in AT over the corresponding regions significant at the 99%, 95%, 90% confidence levels, respectively. See methods for the specific areas of different regions. Before calculating PDF in **(e–g)**, normalized HWI is standardized by subtracting the average and dividing the standard deviation obtained from the period of 1979–2000.

which is probably related to the simulated spatial patterns of AT changes.

### Accelerated increasing trend in European heatwaves

Next, we analyze the accelerated trends over Europe to epitomize how the heterogeneous HWI trends are linked to the complex AT changes. Western and Eastern Europe are selected as examples because the strong upward trends in European heatwaves reach the highest peak among those over all subcontinents in the Northern Hemisphere (Fig. 3a and Supplementary Fig. S1a).

Figure 4a, b exhibit the observed zonally asymmetric trends in high-pressure and low-pressure cumulative intensities, respectively. Accelerated trends in high-pressure extremes are observed over Europe, Eastern Asia and Western North America, while low-pressure ones increase over the Northeastern Atlantic, northern Africa, central Asia, the Japan Sea and Eastern North America. The acceleration of increasing trends in European heatwaves is tied to more intense local high-pressure extremes, especially over Eastern Europe (Fig. 4a, c, d). In addition to local co-variability between surface warming and tropospheric high-pressure activity, the accelerated increasing European HWI trends are also accompanied by remote intensified trends in low-pressure anomalies. For Western Europe, about two-third of the remote most-connected low-pressure grid cells are located over the Northeastern Atlantic and northern Africa, where low-pressure intensities increase significantly (Fig. 4b, c). The intensified low-pressure anomalies over

both regions may result in more heatwaves over Western Europe via an enhanced warm advection by southerly wind<sup>42,43</sup> (Fig. 4b). By contrast, for Eastern Europe, 77% of the most-linked low-pressure areas are observed over central Asia-central Russia, where low-pressure intensity becomes higher during the last four decades (Fig. 4b, and d). The fast-increasing heatwave intensity over Eastern Europe is tied to magnified AT from Eastern Europe to central Asia-central Russia in the east (Fig. 4b).

The amplified atmospheric wave trains and their linkages to accelerated European HWI trends are further confirmed by an empirical orthogonal function (EOF; see Methods for details) analysis. We perform EOF analysis on Western-Europe extended region and Eastern-Europe extended region shown in Fig. 4e, f, which cover most of the most-connected pressure-extreme grid cells for Western European and Eastern European heatwaves, respectively (Fig. 4c, d). The first leading mode of the 500-hPa meridional wind (V500) over Western-Europe extended region is characterized by cyclonic anomalies over the Northeastern Atlantic and northern Africa, and anticyclonic anomalies over Western Europe (Fig. 4e). A significant intensification of this mode promotes the formation of more intense heatwaves over Western Europe but reduces the heatwave intensity over northern Africa and Eastern Europe (Fig. 4e and g). Similarly, the first EOF mode of V500 over the Eastern-Europe extended region indicates a magnified atmospheric wave train propagates eastward from Eastern Europe to central Asia-central Russia, and favor the amplification of Eastern European HWI

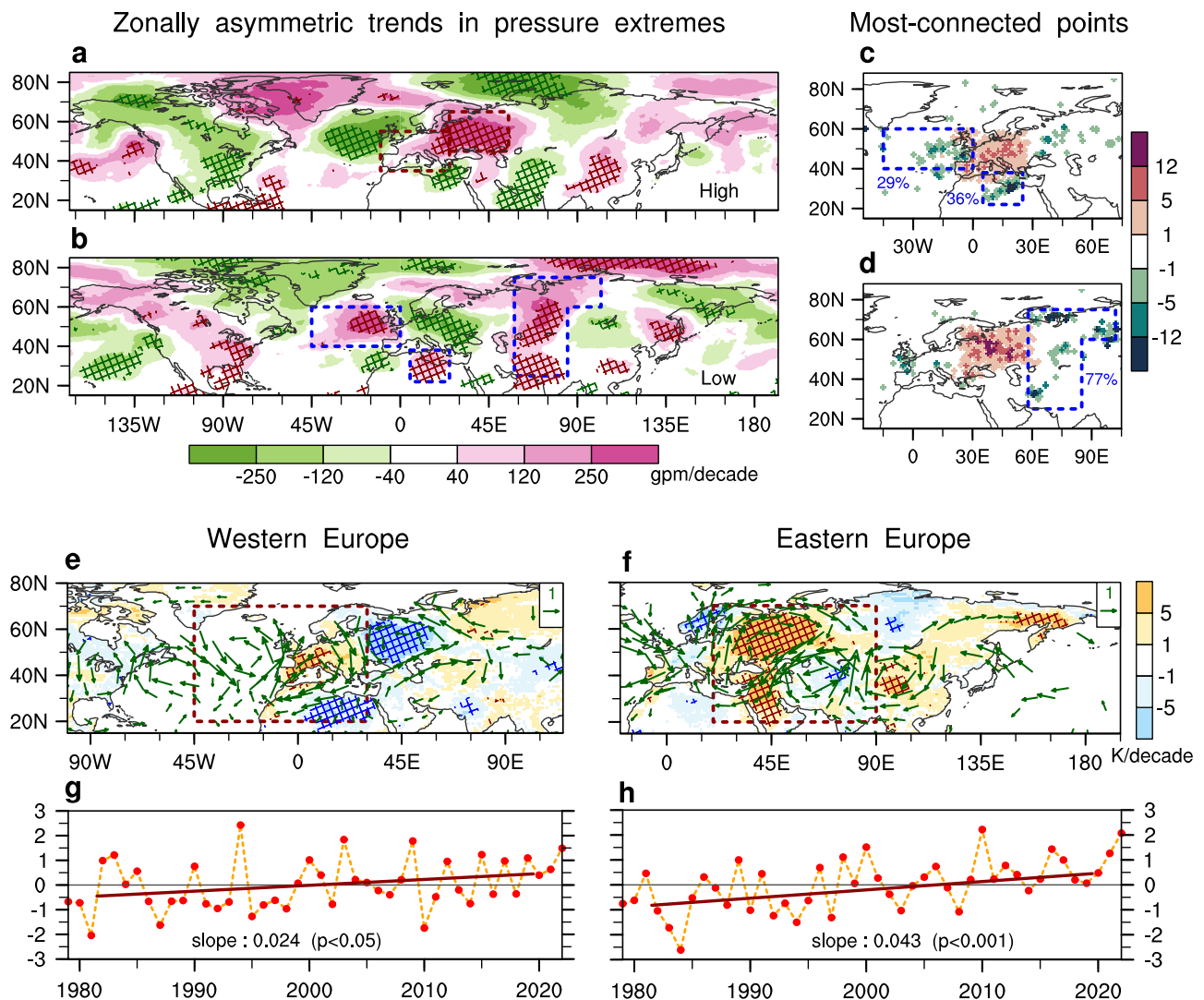


**Fig. 4 | Accelerated increasing trends in European heatwaves linked to the amplified atmospheric teleconnections (AT).** Observed zonally asymmetric trends (units:  $\text{gpm decade}^{-1}$ ) in (a) high-pressure intensity and (b) low-pressure intensity. Number of most-connected high-pressure (red markers) and low-pressure (green markers) grid cells (units: 1) for (c) Western and (d) Eastern European heatwaves. Normalized time series of **g**  $PC_{west}$  and **h**  $PC_{east}$ , which are the principal components associated to the leading EOF mode for V500 over the Western-Europe extended region ( $20^{\circ}$ – $70^{\circ}$ N,  $45^{\circ}$ W– $30^{\circ}$ E) and Eastern-Europe extended region ( $20^{\circ}$ – $70^{\circ}$ N,  $20^{\circ}$ – $90^{\circ}$ E), respectively. Regressed patterns of heatwave cumulative intensity (HWI; shadings; units: K) and atmospheric circulations at

500 hPa (vectors; units:  $\text{m s}^{-1}$ ) onto **e**  $PC_{west}$  and **f**  $PC_{east}$ . Significant trends ( $p < 0.1$ ) and significant anomalies ( $p < 0.05$ ) are hatched in (a, b) and (e, f), respectively. Only the significant atmospheric circulations ( $p < 0.05$ ) are plotted in (e, f). Western Europe (WE;  $35^{\circ}$ – $55^{\circ}$ N,  $10^{\circ}$ W– $25^{\circ}$ E) and Eastern Europe (EE;  $45^{\circ}$ – $65^{\circ}$ N,  $25^{\circ}$ – $55^{\circ}$ E) are outlined by the red boxes in (a). Northeastern Atlantic ( $40^{\circ}$ – $60^{\circ}$ N,  $45^{\circ}$ W– $0^{\circ}$ ), northern Africa ( $22^{\circ}$ – $38^{\circ}$ N,  $5^{\circ}$ – $25^{\circ}$ E), central Asia-central Russia ( $25^{\circ}$ – $60^{\circ}$ N,  $58^{\circ}$ – $85^{\circ}$ E, and  $60^{\circ}$ – $75^{\circ}$ N,  $58^{\circ}$ – $102^{\circ}$ E) are outlined by the blue boxes in (b–d). The red boxes in (e, f) present the domains of Western-Europe extended region and Eastern-Europe extended region for EOF analysis.

trends (Fig. 4f and h). The atmospheric signals are complex because two types of aforementioned intensified Rossby wave trains favor opposite tendencies of European HWI. How can we evaluate the Eastern European HWI trend, if it was intensified as one type of wave train become stronger, but was weakened as the other type of wave train was also enhanced? The network-based AT measure provides a comprehensive understanding and quantifications. Our network-searching results reveal that Western European HWI are most likely linked to atmospheric variations over the northeastern Atlantic and northern Africa, while Eastern European HWI tied to that over central Asia-central Russia (Fig. 4c, d). Therefore, accelerated increasing trends in Western and Eastern European HWI, are closely linked to magnified atmospheric wave trains from northeastern Atlantic to North Africa (Fig. 4e and g), and from Eastern Europe to central Asia (Fig. 4f and h), respectively.

### Role of AT changes in simulation of spatially heterogeneous trends in heatwaves via CMIP6 models

Simulated dependences between zonally asymmetric trends in heatwave intensity and AT changes are examined in the historical period of 1979–2014 by 29 CMIP6 models (listed in Supplementary Table 1).

Individual models capture the correct signs of asymmetric HWI trends over some regions compared to the ERA5 reanalysis dataset, but fail over other regions (see Supplementary Figs. S9 and S10), probably due to the challenging reproduction of the complex atmospheric circulation changes. For Eastern European heatwaves, most models well reproduce the accelerated trends, whereas eight models fail to simulate the correct signs of the asymmetric HWI trends (Fig. 5c, Supplementary Figs. S9 and S10). Eight models simulating the highest accelerated trends over Eastern Europe and

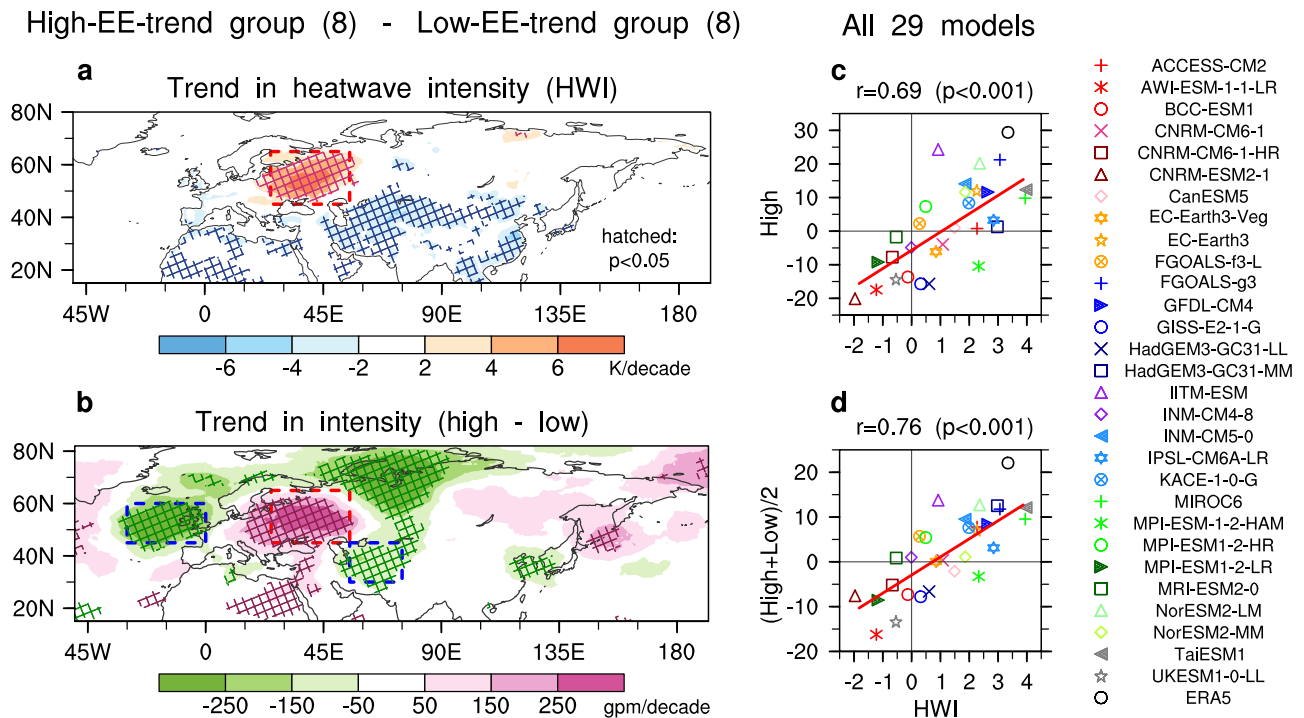


**Fig. 5 | Simulated trends in Eastern European heatwaves linked to the atmospheric teleconnections (AT) in CMIP6 models.** Simulated differences in zonally asymmetric trends between the high-EE-trend group and the low-EE-trend group for **a** the heatwave cumulative intensity (HWI; units: K decade<sup>-1</sup>) and **b** the difference between high-pressure and low-pressure intensities (units: gpm decade<sup>-1</sup>). The high-EE-trend (low-EE-trend) group includes 8 models simulating the highest (lowest) Eastern European asymmetric HWI trends. Significant differences ( $p < 0.05$ ) are hatched in **(a, b)**. Simulated zonally asymmetric trends in HWI versus **c** high-pressure intensity, and **(d)** mean intensities between high-pressure and low-

pressure extremes in 29 CMIP6 models. Results obtained from the ERA5 reanalysis dataset are also provided in **(c, d)**. The high-pressure intensity in **(c, d)** is averaged over Eastern Europe (45°–65°N, 25°–55°E), while the low-pressure intensity is averaged over the northeastern Atlantic (45°–60°N, 30°W–0°) and Western Asia (30°–45°N, 55°–75°E). The x-axis units for **(c, d)** are K decade<sup>-1</sup>, while the y-axis units are gpm year<sup>-1</sup>. The red boxes in **(a, b)** present the domain of Eastern Europe, while blue boxes in **(b)** present the domains of Northeastern Atlantic and Western Asia. The labels denoting the 29 models and the ERA5 trends are shown in the rightmost corner.

the other eight model simulating the negative asymmetric trends are picked out for a composite analysis (see Methods for details about the high-EE-trend group and low-EE-trend group). The high-EE-trend group is likely to reproduce an intensified atmospheric wave train with locally increased high-pressure intensities over Eastern Europe, and increased low-pressure intensities over northeastern Atlantic and Western Asia, and vice versa for the low-EE-trend group (Fig. 5a, b, Supplementary Figs. S10–S13).

Among the 29 models, significant positive correlations of the simulated trends in heatwaves over Eastern Europe with those in local high-pressure intensities, and those in AT intensities, are observed (Fig. 5c, d). Here, AT intensities are simply identified as the average of high-pressure intensity over Eastern Europe and the low-pressure intensity over northeastern Atlantic and Western Asia. The correlation between HWI and AT intensity is even higher than that with local high-pressure trends (Fig. 5c, d), indicating that it is necessary to include the potential influences of remote low-pressure intensity as a part of AT when investigating the local heatwave variability. These results suggest the critical role of the reproduced changing AT in simulating the spatially nonuniform heatwave trends. That is, the stronger the AT changes simulated by a model, the higher the Eastern European HWI increase is displayed in this model. A similar analysis, but for Western Europe, reveals that reproducing the Western European heatwave trends also relies on the simulations of Western-European-heatwave-related AT patterns (see Supplementary information text and Fig. S14). The close dependence between HWI and AT in historical simulations also highlights the potential significant impacts of the simulated AT shifts on the projected heatwaves in future scenarios.

## Discussion

This study quantifies the close linkage between the heterogeneous upward trends in heatwave intensity and the AT shifts in the Northern Hemisphere. By means of a complex network analysis, we discover that in addition to coinciding with local tropospheric high-pressure extremes, heatwaves occur concurrently with remote cold and low-pressure extremes at a distance of approximately 2700 kilometers. Therefore, a quantitative AT index is identified at each grid cell as the averaged intensities of most-connected local (<1500 km) high-pressure extremes and remote (1500–4000 km) low-pressure extremes.

Explicitly, about half of the HWI interannual variability is linked to AT variations in the middle and higher latitudes, and the correct signs of zonally asymmetric HWI trends are estimated by AT changes in nearly 80% of the mid-latitude land area. In particular, an intensified AT explains nearly 70% of the zonally asymmetric accelerated HWI trends over Eastern Europe, and above 50% over Western Europe. For other regions, about or more than 30% of the zonally asymmetric HWI trends are explained by AT shifts. It is highlighted in this study that zonally asymmetric warming caused by changing atmospheric circulations should be given great importance, on account of which the zonally uniform warming known as thermodynamic changes<sup>17,18</sup> could be doubled or offset by the modulations of AT shifts.

In contrast, a single CGT index<sup>44</sup> could just estimate the correct signs of about 45% land areas in all latitudes for zonally asymmetric HWI trends and estimate regrettably an opposite trend over Western Europe (see Supplementary Fig. S15). Only the accelerated trends over Eastern Europe and Eastern Asia can be well estimated by this CGT index, possibly because of the complex dominances by diverse AT

signals over distinct regions. Other regions might be affected by other atmospheric wave train indices with different phases and wavenumbers. This emphasizes the essential role of network-searching and grid-based measures in the investigations of complex AT variations and their connections with the heterogeneous HWI trends.

There are still problems unsolved. Our results show that the simulated asymmetric HWI trends largely rely on the fidelity in representing the AT changes in CMIP6 models. However, the spatial heterogeneity of future projected heatwave intensifications and their linkages to AT changes have not been investigated, although heatwave increase in a global scale projected by almost all climate models have been widely studied<sup>2</sup>. Considering only the future-projected global average of heatwave trends may seriously underestimate the regional heatwave risks amplified by enhanced AT over future hotspot regions.

In addition, we consider temperature extremes and atmospheric pressure extremes, but other climate extremes have not been discussed in this study. Extreme rainfall may play a vital role in modulating the atmospheric circulation through releasing condensational heat. Previous studies have found that extreme rainfall over Pakistan with strong latent heat release could modulate the occurrences of extreme heatwaves over Eastern Asia<sup>39,45</sup>. Based on a network analysis, occurrences of heatwaves are observed simultaneously and significantly over the east of extreme rainfall events in a distance of roughly 2,100 km (see Supplementary information text and Fig. S16). The nature behind the concurrent heatwaves and extreme rainfall deserves thorough researches, which are not investigated in detail in this paper. Furthermore, the potential impacts of soil moisture deficit<sup>36,46–52</sup> as well as the compound heatwave-moisture extremes<sup>53–57</sup>, including heat-dry<sup>54,55</sup> and heat-humid<sup>56,57</sup> extremes, are not discussed in this study. Soil moisture deficit is another driver that we do not include in this study, but it can modulate heatwave variability through altering the surface latent flux and thus reducing the evaporative cooling<sup>36,46–48</sup>. It could even feed back onto the large-scale atmospheric circulation<sup>36,49–52</sup>. A thorough quantification of the spatial disparity in compound extreme changes, probably attributed to interactive AT shifts and soil moisture changes, is conducive to addressing the potential risks more precisely.

## Methods

### Datasets

The atmospheric variables derived from the European Centre for Medium-range Weather Forecasts Reanalysis v5 (ERA5) datasets<sup>34</sup>, with a horizontal resolution of  $1^\circ \times 1^\circ$ , are analyzed in this study. Daily  $T_{\max}$  and  $T_{\text{ave}}$  are derived from the maximum and the average of hourly 2-m air temperature ( $T_{2m}$ ) in each day, respectively. Apart from this, hourly variables on 5 pressure levels (600, 500, 400, 300, and 200 hPa), including zonal wind ( $u$ ), meridional wind ( $v$ ), and geopotential height, are averaged into daily means before further analysis. The study period for the ERA5 reanalysis dataset is limited to June–July–August (JJA) during the satellite era (1979–2022). The research area is the Northern Hemisphere, in which the near-equatorial areas ( $0$ – $10^\circ\text{N}$ ) are excluded from this study because JJA is not the hottest season for these areas.

In addition, daily maximum near-surface air temperature ( $T_{\max}$ ) and 500-hPa geopotential height ( $H500$ ) from the CMIP6 historical simulations<sup>35</sup> during 1979–2014 are examined in this study. The output of each model simulation is interpolated into  $1^\circ \times 1^\circ$  before analysis. Twenty-nine CMIP6 models are included: ACCESS-CM2, AWI-ESM1-1-LR, BCC-ESM1, CNRM-CM6-1, CNRM-CM6-1-HR, CNRM-ESM2-1, CanESM5, EC-Earth3-Veg, EC-Earth3, FGOALS-f3-L, FGOALS-g3, GFDL-CM4, GISS-E2-1-G, HadGEM3-GC31-LL, HadGEM3-GC31-MM, IITM-ESM, INM-CM4-8, INM-CM5-0, IPSL-CM6A-LR, KACE-1-0-G, MIROC6, MPI-ESM1-2-HAM, MPI-ESM1-2-HR, MPI-ESM1-2-LR, MRI-ESM2-0, NorESM2-LM, NorESM2-MM, TaiESM1, and UKESM1-0-LL (see Supplementary Table 1).

### Definition of weather extremes

Heatwaves are identified over land grids when daily  $T_{\max}$  exceeds its 90<sup>th</sup> percentile threshold ( $\theta_{90th}$ ) of the reference period of 1981–2010 for at least 3 consecutive days. The  $\theta_{90th}$  for a specific day is derived from a total of 30 years  $\times$  15 days (7 days on either side of the target day). For instance, the threshold value on 16 June is equivalent to the 90<sup>th</sup> percentile of  $T_{\max}$  on 9–23 June during 1981–2010. On the other hand, cold extremes are recognized over the land grids when  $T_{\text{ave}}$  reaches below  $\theta_{10th}$  for at least 3 consecutive days. The definition of  $\theta_{10th}$  is similar to  $\theta_{90th}$ , but for the 10<sup>th</sup> percentile threshold of  $T_{\text{ave}}$ . High-pressure (low-pressure) extremes are selected when the geopotential height anomalies at 500 hPa ( $H500_{\text{ano}}$ ) are higher (lower) than one standard deviation ( $\sigma$ ). For each day, the climatology and standard deviation  $\sigma$  are derived from a 30-year time series (1981–2010).

Cumulative intensities of heatwave (HWI), cold extreme, high-pressure extreme, and low-pressure extreme are defined as the accumulated values  $HWI = \sum(T_{\max} - \theta_{90th, \max})$ ,  $Cold = \sum(\theta_{10th, \text{ave}} - T_{\text{ave}})$ ,  $High = \sum(H500_{\text{ano}})$ , and  $Low = \sum(-H500_{\text{ano}})$ , respectively, for the corresponding type of extremes in each year.

### Network analysis

For each network, the strength of a link between grid points  $a$  and  $b$  is denoted as  $L_{(a,b)}$ . It is defined as the total number of concurrent days when a heatwave occurs over  $a$  and another heatwave (cold extreme) occurs over  $b$  simultaneously, for heat-heat (heat-cold) daily concurrence network. For heat-high (heat-low) daily concurrence network,  $L_{(a,b)}$  is identified as the total number of concurrent days when a heatwave occurs over  $a$  and a high-pressure (low-pressure) extreme occurs over  $b$  simultaneously. We do not consider time lag when counting the number of the concurrent days between weather extremes occurring over the two grid cells (see Supplementary Fig. S3) in this study.

We shuffle the time series of daily extremes (presence as 1 or absence as 0) 1000 times for each grid cell, and then calculate the 99<sup>th</sup> percentile of  $L_{(a,b)}$  for each pair of grid cells ( $a,b$ ) from the shuffled data. In the following, we conduct significant test for the links in the four daily concurrence networks. When the real  $L_{(a,b)}$  is lower than the 99<sup>th</sup> percentile threshold, this link is identified as insignificant and will be removed.

For the heat-high (heat-low) interannual correlation network,  $L_{(a,b)}$  is defined as the Pearson's correlation coefficient  $R$  between HWI and the high-pressure (low-pressure) extreme cumulative intensity. All the temporal linear trends of yearly time series are removed before calculating  $R$ . Only the significant positive links, i.e.,  $L_{(a,b)} = R > 0.297$  ( $p < 0.05$ ), will be retained.

One of the commonly used two-layer network coefficients, cross-degree centrality<sup>58–60</sup> is used to quantify the topological characteristics of heatwaves-atmospheric circulation relationships. Cross-degree centrality inside regional heatwaves is the sum of strength of all significant links to the grid cells within the region:  $D_b = \sum_{a \in R} L_{(a,b)}$ . High cross-degree centrality  $D_b$  inside region- $R$  heatwaves indicates the area with high occurrences of pressure extremes over grid cell  $b$  when heatwaves occur over region  $R$ . For instance, high-value shading (contour) region indicates the area with high occurrences of high-pressure (low-pressure) extremes when heatwaves occur within the corresponding box regions (Fig. 2c and f).

### Composite analysis for Eastern and Western European heatwave events

Eastern European heatwave days are recognized when the number of heatwave land grid points reaches above 90<sup>th</sup> percentile (i.e.,  $\geq 137$  grid cells, 23.4 % of the total 585 grid cells) over  $45^\circ$ – $65^\circ\text{N}$ ,  $25^\circ$ – $55^\circ\text{E}$ , which accounts for about 10% (405 days) of the total 4048 summer days. Similarly, Western European heatwave days are identified when heatwaves occur in no less than 88 land grid points (i.e.,  $\geq 88$  grid cells, 19.8



% of the total 445 land grid cells) over 35°–55°N, 10°W–25°E, so that about 10% (412 days) of the summer days are picked out as the regional heatwave days.

Composite anomalies are the differences between the average of the physical variables in regional heatwave days (406 days for Eastern Europe and 410 days for Western Europe) and the climatology (4048 days). The statistical significance level (i.e.,  $p < 0.05$ ) of composite anomalies is calculated by the Student's  $t$ -test.

Eastern and Western European heatwave events based on the 95th percentile threshold are also analyzed (see Supplementary information text and Fig. S17). Similar patterns of  $T_{ave}$  and H500 are obtained for the composite analysis of regional heatwaves based on both 90th and 95th percentile thresholds.

### Wave activity flux

The propagation of atmospheric Rossby waves can be described by the wave activity flux (known as TN flux<sup>61</sup>), which can be written as follows:

$$W = \frac{p \cos \varphi}{2 |\bar{U}|} \left[ \begin{aligned} & \frac{\bar{u}}{a^2 \cos^2 \varphi} \left( \frac{\partial \psi'}{\partial \lambda} \right)^2 - \psi' \frac{\partial^2 \psi'}{\partial \lambda^2} + \frac{\bar{v}}{a^2 \cos \varphi} \left( \frac{\partial \psi'}{\partial \lambda} \frac{\partial \psi'}{\partial \varphi} - \psi' \frac{\partial^2 \psi'}{\partial \lambda \partial \varphi} \right) \\ & \frac{\bar{u}}{a^2 \cos \varphi} \left( \frac{\partial \psi'}{\partial \lambda} \frac{\partial \psi'}{\partial \varphi} - \psi' \frac{\partial^2 \psi'}{\partial \lambda \partial \varphi} \right) + \frac{\bar{v}}{a^2} \left( \left( \frac{\partial \psi'}{\partial \varphi} \right)^2 - \psi' \frac{\partial^2 \psi'}{\partial \varphi^2} \right) \end{aligned} \right] \quad (1)$$

where  $p$  = pressure (per 1000 hPa), while  $\varphi$ ,  $\lambda$ , and  $a$  are latitude, longitude, and the earth radius, respectively. Besides,  $\psi'$  represents the anomaly of the stream function, while  $\bar{U}$ ,  $\bar{u}$ , and  $\bar{v}$  indicate the climatology of the wind speed, zonal wind, and meridional wind, respectively.

### Searching most-connected grids and identifying atmospheric teleconnections

For each grid cell  $a$ , we search the two most-connected high-pressure grid cells  $i$  and  $j$ , and the two most-connected low-pressure grid cells  $m$  and  $n$ . For grid cell  $i$  ( $j$ ), the high-pressure extreme has the highest yearly correlation coefficient (daily concurrence) with the heatwave over grid cell  $a$ . For grid cell  $m$  ( $n$ ), the low-pressure extreme has the highest yearly correlation (daily concurrence) with the heatwave over grid cell  $a$ . When the strongest link between a heat-extreme grid cell and all pressure-extreme grid cells are found, the associated pressure extreme time series are used to measure the AT strength for the corresponding heatwave grid cell. Interannual correlation and daily concurrence networks are both included to identify AT index on account of the complicated atmospheric signals with dissimilar variations. To guarantee the real physical representations of the AT measure, we limit the geographical distance of the links when searching the most-connected grid cells. For most-connected high-pressure grid cell  $i$  ( $j$ ), the distance between  $a$  and  $i$  ( $j$ ) is less than 1500 km. For most-connected low-pressure grid cell  $m$  ( $n$ ), the distance between  $a$  and  $m$  ( $n$ ) is between 1500 km and 4000 km.

$$distance(a, i) < 1500 \text{ km}, distance(a, j) < 1500 \text{ km} \quad (2)$$

$$distance(a, m) \in 1500 - 4000 \text{ km}, distance(a, n) \in 1500 - 4000 \text{ km} \quad (3)$$

At each grid cell  $a$ , the strength of yearly AT is defined as the average of high-pressure cumulative intensities over  $i$  and  $j$  and low-pressure cumulative intensities over  $m$  and  $n$ . The zonal mean of the high-pressure and low-pressure cumulative intensities has been removed to excludes the potential influences of global uniform

warming.

$$AT_a = (High_i + High_j + Low_m + Low_n)/4 \quad (4)$$

In general, AT includes covariant atmospheric signals with long geographical distances. Therefore, both local high-pressure intensities and remote low-pressure intensities are directly included to identify the strengths of heatwave-related AT. Nevertheless, the results for AT measures using only local high-pressure intensities are also supplied (see Supplementary information text and Fig. S8). Overall, the dipolar AT index including both local high-pressure and remote low-pressure intensities, exhibits a stronger interannual linkage with heatwaves in the Northern Hemisphere, compared with the only local high-pressure index.

### Zonally asymmetric trends and estimated trends

The zonally asymmetric trends are the zonal deviations from the zonal means of heatwave, high-pressure, and low-pressure intensity trends. The zonal mean of HWI is preprocessed by conducting 31-degree moving mean to remove the discontinuity caused probably by the sharp changes in the land proportion at different latitudes (see Supplementary Fig. S1).

In addition, we estimate the HWI trends based on AT changes at each grid point by using a linear regression model:

$$Trend_{(HWI, estimated)} = RC_{(AT, HWI)} \times Trend_{AT} \quad (5)$$

where  $RC$  is the regression coefficient between the detrended yearly time series of AT and HWI.

Regional zonally asymmetric and estimated trends are averaged over these regions: Northwestern North America (NWNNA; 60°–75°N, 160°–100°W), Eastern North America (ENA; quadrangle, bottom 30°N, 92°–70°W, upper 45°N, 112°–70°W), Western Europe (WE; 35°–55°N, 10°W–25°E), Eastern Europe (EE; 45°–65°N, 25°–55°E), Europe (Western Europe and Eastern Europe), South Asia-central Asia (22°–45°N, 65°–80°E), Eastern Asia (EA; 28°–34°N, 100°–120°E), and Northeastern Asia (NEA; quadrangle, bottom 50°N, 115°–160°E, upper 75°N, 140°–160°E).

### Sensitivity test

Four additional definitions of pressure extremes are used to identify the geographical distance feature and the grid-based heatwave-AT linkage. At three pressure levels, geopotential height anomaly at 850 hPa (H850 anomaly), 500 hPa (H500 anomaly), and 200 hPa (H200 anomaly) are analyzed to recognize high-pressure and low-pressure extremes. The four definitions include: (1) H850 anomaly exceeds one standard deviation, (2) H200 anomaly exceeds one standard deviation, (3) H500 anomaly exceeds 1.5 standard deviation, (4) H500 exceeds the 90<sup>th</sup> percentile or 10<sup>th</sup> percentile threshold for at least 3 consecutive days, which are similar as the definition of heatwaves using  $T_{max}$  but for pressure extremes using H500.

The distance distributions of concurrent heatwave-pressure extremes are similar for all the four definitions (see Supplementary Figs. S18 and S19). The interannual explained variances between HWI and AT reach nearly 50% in the mid-latitudes for the pressure extremes based on all definitions except for which is slightly lower (~40%) at 850 hPa (see Supplementary Figs. S20 and S21). It is probably because atmospheric wave trains almost propagate along the westerly jet streams in the middle and upper troposphere.

In addition, we investigate the probability density function of strong, medium, and weak significant links corresponding to different thresholds (see Supplementary Figs. S6). For strong links between heatwaves and high-pressure extremes, the second peak (~5500 km) is much weaker than the strongest peak (< 1500 km). Western European heatwaves are even not significantly correlated with the remote

high-pressure anomalies in a distance of 5200–6000 km because the correlation decreases rapidly when the geographical distance increases (Fig. 2d, e). Therefore, we are concentrated on the strongest local high-pressure and the strongest remote low-pressure grid cells, and use them to identify the strengths of heatwave-related atmospheric teleconnection.

### EOF analysis

To investigate the changes in regional atmospheric circulation patterns, an empirical orthogonal function (EOF) analysis is performed for the yearly anomalies of 500-hPa meridional winds (V500) during the JJAs of 1979–2022. For Western Europe, the first EOF mode for the V500 over Western Europe-extended region (20°–70°N, 45°W–30°E) is analyzed and  $PC_{west}$  is the associated principal component (Fig. 4g). For Eastern Europe, the first EOF mode for the V500 over Eastern Europe-extended region (20°–70°N, 20°–90°E) is analyzed and  $PC_{east}$  is the associated principal component (Fig. 4h). The domains of Western Europe-extended region and Eastern Europe-extended region are shown in Fig. 4e, f, which cover most of the most-connected pressure-extreme grid cells for Western European and Eastern European heatwaves, respectively (Fig. 4c, d).

In addition, a circum-global teleconnection (CGT) pattern is also derived based on the EOF analysis, following previous studies<sup>18,44</sup>. It is identified as the first leading mode of 200-hPa meridional winds (V200) over 20°–60°N, 0°–150°E, given that its major characteristics are observed near the Asian jet stream. The CGT pattern is characterized by alternative cyclonic and anticyclonic circulation anomalies across the Eurasian continent<sup>18,44</sup>. In particular, blocking anticyclones are located over Eastern Europe and Eastern Asia, while cyclonic circulation anomalies over Western Europe and central Asia (see Supplementary Fig. S15a). The CGT index is defined as the associated principal component (see Supplementary Fig. S15d).

### Composite analysis for simulation of the highest accelerated and the lowest asymmetric trends over Eastern Europe

Eight models simulating the highest accelerated HWI trends over Eastern Europe include FGOALS-g3, GFDL-CM4, HadGEM3-GC31-MM, IPSL-CM6A-LR, MIROC6, MPI-ESM1-2-HAM, NorESM2-LM, and TaiESM1. The eight models are picked out into a category, which is named as the high-EE-trend group. Similarly, the low-EE-trend group includes eight models simulating the lowest asymmetric trends over Eastern Europe: AWI-ESM1-1-LR, BCC-ESM1, CNRM-CM6-1-HR, CNRM-ESM2-1, INM-CM4-8, MPI-ESM1-2-LR, MRI-ESM2-0, and UKESM1-0-LL. To examine the simulated dependences between HWI and AT, we conduct composite analysis by averaging the zonally asymmetric trends in both HWI and the difference between high-pressure and low-pressure intensities simulated by the 16 models in high-EE-trend group and low-EE-trend group shown in Fig. 5a, b and Supplementary Fig. S13.

### Data availability

The ERA5 single-level and multi-level variables<sup>34</sup> could be freely downloaded from <https://doi.org/10.24381/cds.adbb2d47> and <https://doi.org/10.24381/cds.bd0915c6>, respectively. The outputs of CMIP6 simulations<sup>35</sup> could be freely obtained from <https://esgf-node.lnl.gov/search/cmip6/>. The processed data used in this study are available in the following Zenodo database: <https://zenodo.org/records/13361912>. Source data are provided with this paper for Figs. 1–5.

### Code availability

The EOF approach and Student's *t*-test are provided by the NCL functions “eofunc” (<https://www.ncl.ucar.edu/Document/Functions/Built-in/eofunc.shtml>) and “ttest” (<https://www.ncl.ucar.edu/Document/Functions/Built-in/ttest.shtml>), respectively. The codes used to generate the results of this study are available at [https://github.com/FenyngCai/heatwave\\_trends-AT-network](https://github.com/FenyngCai/heatwave_trends-AT-network).

## References

- Coumou, D. & Rahmstorf, S. A decade of weather extremes. *Nat. Clim. Change* **2**, 491–496 (2012).
- Coumou, D. & Robinson, A. Historic and future increase in the global land area affected by monthly heat extremes. *Environ. Res. Lett.* **8**, 034018 (2013).
- Christidis, N., Jones, G. S. & Stott, P. A. Dramatically increasing chance of extremely hot summers since the 2003 European heatwave. *Nat. Clim. Change* **5**, 46–50 (2015).
- Mazdiyasni, O. & AghaKouchak, A. Substantial increase in concurrent droughts and heatwaves in the United States. *Proc. Natl Acad. Sci. USA.* **112**, 11484–11489 (2015).
- Meehl, G. A. & Tebaldi, C. More intense, more frequent, and longer lasting heat waves in the 21st century. *Science* **305**, 994–997 (2004).
- Perkins-Kirkpatrick, S. E. & Lewis, S. C. Increasing trends in regional heatwaves. *Nat. Commun.* **11**, 3357 (2020).
- Perkins, S. E., Alexander, L. V. & Nairn, J. R. Increasing frequency, intensity and duration of observed global heatwaves and warm spells. *Geophys. Res. Lett.* **39**, 20 (2012).
- Nangombe, S. et al. Record-breaking climate extremes in Africa under stabilized 1.5 °C and 2 °C global warming scenarios. *Nat. Clim. Change* **8**, 375–380 (2018).
- Ballester, J. et al. Heat-related mortality in Europe during the summer of 2022. *Nat. Med.* **29**, 1857–1866 (2023).
- Bartusek, S., Kornhuber, K. & Ting, M. 2021 North American heatwave amplified by climate change-driven nonlinear interactions. *Nat. Clim. Change* **12**, 1143–1150 (2022).
- Benfield, A. *Global catastrophe recap September 2021 (PDF)*. (Report). p. 13. Retrieved from <http://thoughtleadership.aon.com/Documents/20210012-analytics-if-september-global-recap> (2021).
- World Meteorological Organization (WMO) 2021. *State of the Global Climate WMO Provisional report*. Available online at [https://library.wmo.int/doc\\_num.php?explnum\\_id=10859](https://library.wmo.int/doc_num.php?explnum_id=10859) (2021).
- Zhang, X. et al. Increased impact of heat domes on 2021-like heat extremes in North America under global warming. *Nat. Commun.* **14**, 1690 (2023).
- Di Capua, G. & Rahmstorf, S. Extreme weather in a changing climate. *Environ. Res. Lett.* **18**, 102001 (2023).
- Coumou, D., Di Capua, G., Vavrus, S., Wang, L. & Wang, S. The influence of Arctic amplification on mid-latitude summer circulation. *Nat. Commun.* **9**, 2959 (2018).
- Rousi, E., Kornhuber, K., Beobide-Arsuaga, G., Luo, F. & Coumou, D. Accelerated Western European heatwave trends linked to more-persistent double jets over Eurasia. *Nat. Commun.* **13**, 3851 (2022).
- Hong, X., Lu, R. & Li, S. Amplified summer warming in Europe–West Asia and Northeast Asia after the mid-1990s. *Environ. Res. Lett.* **12**, 094007 (2017).
- Wang, L., Xu, P., Chen, W. & Liu, Y. Interdecadal variations of the Silk Road pattern. *J. Clim.* **30**, 9915–9932 (2017).
- Ren, L., Zhou, T. & Zhang, W. Attribution of the record-breaking heat event over Northeast Asia in summer 2018: the role of circulation. *Environ. Res. Lett.* **15**, 054018 (2020).
- Di Capua, G. et al. Drivers behind the summer 2010 wave train leading to Russian heatwave and Pakistan flooding. *npj Clim. Atmos. Sci.* **4**, 55 (2021).
- Kornhuber, K. et al. Extreme weather events in early summer 2018 connected by a recurrent hemispheric wave-7 pattern. *Environ. Res. Lett.* **14**, 054002 (2019).
- Kornhuber, K. et al. Amplified Rossby waves enhance risk of concurrent heatwaves in major breadbasket regions. *Nat. Clim. Change* **10**, 48–53 (2020).
- Liu, Y., Sun, C. & Li, J. The boreal summer zonal wavenumber-3 trend pattern and its connection with surface enhanced warming. *J. Clim.* **35**, 833–850 (2022).

24. Zhang, T. et al. Interannual variability of springtime extreme heat events over the southEastern edge of the Tibetan Plateau: Role of a spring-type circumglobal teleconnection pattern. *J. Clim.* **34**, 9915–9930 (2021).
25. Zhang, T. et al. Influences of the boreal winter Arctic Oscillation on the peak-summer compound heat waves over the Yangtze–Huaihe River basin: the North Atlantic capacitor effect. *Clim. Dyn.* **59**, 2331–2343 (2022).
26. Vautard, R. et al. Heat extremes in Western Europe increasing faster than simulated due to atmospheric circulation trends. *Nat. Commun.* **14**, 6803 (2023).
27. Boers, N., Bookhagen, B., Marwan, N. & Kurths, J. & Marengo, J. Complex networks identify spatial patterns of extreme rainfall events of the South American Monsoon System. *Geophys. Res. Lett.* **40**, 4386–4392 (2013).
28. Boers, N., Bookhagen, B., Barbosa, H. M., Marwan, N. & Kurths, J. & Marengo, J. A. Prediction of extreme floods in the Eastern Central Andes based on a complex networks approach. *Nat. Commun.* **5**, 5199 (2014).
29. Boers, N. et al. Complex networks reveal global pattern of extreme-rainfall teleconnections. *Nature* **566**, 373–377 (2019).
30. Mondal, S. & Mishra, A. K. Complex networks reveal heatwave patterns and propagations over the USA. *Geophys. Res. Lett.* **48**, e2020GL090411 (2021).
31. Luo, M. et al. Two different propagation patterns of spatiotemporally contiguous heatwaves in China. *npj Clim. Atmos. Sci.* **5**, 89 (2022).
32. Carney, M. & Kantz, H. Robust regional clustering and modeling of nonstationary summer temperature extremes across Germany. *Adv. Stat. Climatol. Meteorol. Oceanogr.* **6**, 61–77 (2020).
33. Mondal, S. et al. Global droughts connected by linkages between drought hubs. *Nat. Commun.* **14**, 144 (2023).
34. Hersbach, H. et al. The ERA5 global reanalysis. *Q. J. R. Meteorol. Soc.* **146**, 1999–2049 (2020).
35. Eyring, V. et al. Overview of the Coupled Model Intercomparison Project Phase 6 (CMIP6) experimental design and organization. *Geosci. Model Dev.* **9**, 1937–1958 (2016).
36. Domeisen, D. I. V. et al. Prediction and projection of heatwaves. *Nat. Rev. Earth Environ.* **4**, 36–50 (2023).
37. Barriopedro, D., García-Herrera, R., Ordóñez, C., Miralles, D. G. & Salcedo-Sanz, S. Heat waves: physical understanding and scientific challenges. *Rev. Geophys.* **61**, e2022RG000780 (2023).
38. Deng, K., Yang, S., Ting, M., Lin, A. & Wang, Z. An intensified mode of variability modulating the summer heat waves in Eastern Europe and northern China. *Geophys. Res. Lett.* **45**, 11–361 (2018).
39. Wang, Z., Luo, H. & Yang, S. Different mechanisms for the extremely hot central-Eastern China in July–August 2022 from a Eurasian large-scale circulation perspective. *Environ. Res. Lett.* **18**, 024023 (2023).
40. Duchez, A. et al. Drivers of exceptionally cold North Atlantic Ocean temperatures and their link to the 2015 European heat wave. *Environ. Res. Lett.* **11**, 074004 (2016).
41. Chen, W. et al. Attribution of recent trends in temperature extremes over China: role of changes in anthropogenic aerosol emissions over Asia. *J. Clim.* **32**, 7539–7560 (2019).
42. Sousa, P. M. et al. Saharan air intrusions as a relevant mechanism for Iberian heatwaves: The record breaking events of August 2018 and June 2019. *Weather Clim. Extremes* **26**, 100224 (2019).
43. Sousa, P. M. et al. Distinct influences of large-scale circulation and regional feedbacks in two exceptional 2019 European heatwaves. *Commun. Earth Environ.* **1**, 48 (2020).
44. Yasui, S. & Watanabe, M. Forcing processes of the summertime circumglobal teleconnection pattern in a dry AGCM. *J. Clim.* **23**, 2093–2114 (2010).
45. Fu, Z. H., Zhou, W., Xie, S. P., Zhang, R. & Wang, X. Dynamic pathway linking Pakistan flooding to East Asian heatwaves. *Sci. Adv.* **10**, eadk9250 (2024).
46. Miralles, D., Teuling, A. & Heerwaarden, C. Mega-heatwave temperatures due to combined soil desiccation and atmospheric heat accumulation. *Nat. Geosci.* **7**, 345–349 (2014).
47. Mueller, B. & Seneviratne, S. I. Hot days induced by precipitation deficits at the global scale. *Proc. Natl Acad. Sci. USA* **109**, 12398–12403 (2012).
48. Quesada, B., Vautard, R., Yiou, P., Hirschi, M. & Seneviratne, S. I. Asymmetric European summer heat predictability from wet and dry southern winters and springs. *Nat. Clim. Change* **2**, 736–741 (2012).
49. Fischer, E., Seneviratne, S., Vidale, P., Lüthi, D. & Schär, C. Soil moisture: atmosphere interactions during the 2003 European summer heat wave. *J. Clim.* **20**, 5081–5099 (2007).
50. Haarsma, R. J., Selten, F., Hurk, B. V., Hazeleger, W. & Wang, X. Drier Mediterranean soils due to greenhouse warming bring easterly winds over summertime central Europe. *Geophys. Res. Lett.* **36**, L04705 (2009).
51. Zampieri, M. et al. Hot European summers and the role of soil moisture in the propagation of Mediterranean drought. *J. Clim.* **22**, 4747–4758 (2009).
52. Orth, R., Dutra, E. & Pappenberger, F. Improving weather predictability by including land surface model parameter uncertainty. *Mon. Weather Rev.* **144**, 1551–1569 (2016).
53. Lesk, C. et al. Compound heat and moisture extreme impacts on global crop yields under climate change. *Nat. Rev. Earth Environ.* **3**, 872–889 (2022).
54. Wang, J. et al. Anthropogenically-driven increases in the risks of summertime compound hot extremes. *Nat. Commun.* **11**, 528 (2020).
55. Wang, J. et al. Anthropogenic emissions and urbanization increase risk of compound hot extremes in cities. *Nat. Clim. Chang.* **11**, 1084–1089 (2021).
56. Zhang, K. et al. Increased heat risk in wet climate induced by urban humid heat. *Nature* **617**, 738–742 (2023).
57. Raymond, C., Matthews, T. & Horton, R. M. The emergence of heat and humidity too severe for human tolerance. *Sci. Adv.* **6**, eaaw1838 (2020).
58. Mondal, S. & Mishra, A. Quantifying the precipitation, evapotranspiration, and soil moisture network’s interaction over global land surface hydrological cycle. *Water Resour. Res.* **60**, e2023WR034861 (2024).
59. Donges, J. F., Schultz, H. C., Marwan, N., Zou, Y. & Kurths, J. Investigating the topology of interacting networks: Theory and application to coupled climate subnetworks. *Eur. Phys. J. B* **84**, 635–651 (2011).
60. Cai, F. et al. Linkage between European and East Asian heatwaves on synoptic scales. *J. Trop. Meteorol.* **30**, 97–105 (2024).
61. Takaya, K. & Nakamura, H. A formulation of a phase-independent wave-activity flux for stationary and migratory quasigeostrophic eddies on a zonally varying basic flow. *J. Atmos. Sci.* **58**, 608–627 (2001).

## Acknowledgements

The authors wish to thank Zhen Su, Long Huo, Mengke Wei, and Jianxin Zhang at the Potsdam Institute for Climate Impact Research, Shuheng Lin, and Haolin Luo at Sun Yat-sen University for useful discussions. S.Y. and T.Z. are supported by the Guangdong Major Project of Basic and Applied Basic Research (Grant 2020B0301030004), the National Natural Science Foundation of China (Grant 42275020, 42105015), the Innovation Group Project of Southern Marine Science and Engineering Guangdong Laboratory (Zhuhai) (311021001), the Natural Science Foundation of Guangdong Province (Grant 2022A1515010659), and the

Guangdong Province Key Laboratory for Climate Change and Natural Disaster Studies (2020B1212060025). F.C., C.L., and K.L. are supported by the China Scholarship Council (CSC) scholarship.

### Author contributions

F.C., T.Z., S.Y., and J.K. conceived and designed the study. F.C. and T.Z. conducted the analysis and drafted the manuscript. C.L., D.G., S.Y., and J.K. provided comments and revised the manuscript. F.C., T.Z., C.L., D.G., S.Y., K.L., and J.K. discussed the scientific interpretation of the results.

### Competing interests

The authors declare no competing interests.

### Additional information

**Supplementary information** The online version contains supplementary material available at <https://doi.org/10.1038/s41467-024-52254-0>.

**Correspondence** and requests for materials should be addressed to Song Yang or Tuantuan Zhang.

**Peer review information** *Nature Communications* thanks Bernat Jiménez-Estève and Somnath Mondal for their contribution to the peer review of this work. A peer review file is available.

**Reprints and permissions information** is available at <http://www.nature.com/reprints>

**Publisher's note** Springer Nature remains neutral with regard to jurisdictional claims in published maps and institutional affiliations.

**Open Access** This article is licensed under a Creative Commons Attribution-NonCommercial-NoDerivatives 4.0 International License, which permits any non-commercial use, sharing, distribution and reproduction in any medium or format, as long as you give appropriate credit to the original author(s) and the source, provide a link to the Creative Commons licence, and indicate if you modified the licensed material. You do not have permission under this licence to share adapted material derived from this article or parts of it. The images or other third party material in this article are included in the article's Creative Commons licence, unless indicated otherwise in a credit line to the material. If material is not included in the article's Creative Commons licence and your intended use is not permitted by statutory regulation or exceeds the permitted use, you will need to obtain permission directly from the copyright holder. To view a copy of this licence, visit <http://creativecommons.org/licenses/by-nc-nd/4.0/>.

© The Author(s) 2024